ACS NANO
Cite This: ACS Nano 2019, 13, 7676−7689
www.acsnano.org
ARTICLE

Chain-Length- and Saturation-Tuned Mechanics of Fluid Nanovesicles Direct Tumor Delivery

Zhuo Dai,[†,‡,#] Miaorong Yu,[‡,§,#] Xin Yi,[*,∥] Zeming Wu,[∥] Falin Tian,[⊥] Yunqiu Miao,[†,‡] Wenyi Song,[‡] Shufang He,[‡] Ejaj Ahmad,[‡] Shiyan Guo,[‡] Chunliu Zhu,[‡] Xinxin Zhang,[‡] Yiming Li,[†] Xinghua Shi,[§,⊥] Rui Wang,[*,†] and Yong Gan[*,‡,§]

[†]School of Pharmacy, Shanghai University of Traditional Chinese Medicine, Shanghai 201203, China
[‡]Shanghai Institute of Materia Medica, Chinese Academy of Sciences, Shanghai 201203, China
[§]University of Chinese Academy of Sciences, Beijing 100049, China
[∥]Beijing Innovation Center for Engineering Science and Advanced Technology, and Department of Mechanics and Engineering Science, College of Engineering, Peking University, Beijing 100871, China
[⊥]CAS Key Laboratory for Nanosystem and Hierarchy Fabrication, CAS Center for Excellence in Nanoscience, National Center for Nanoscience and Technology, Chinese Academy of Sciences, Beijing 100190, China

Supporting Information

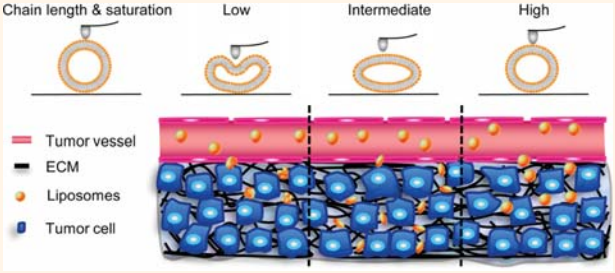

ABSTRACT: **Small unilamellar vesicles (SUVs), ubiquitous in organisms, play key and active roles in various biological processes. Although the physical properties of the constituent lipid molecules (*i.e.*, the acyl chain length and saturation) are known to affect the mechanical properties of SUVs and consequently regulate their biological behaviors and functions, the underlying mechanism remains elusive. Here, we combined theoretical modeling and experimental investigation to probe the mechanical behaviors of SUVs with different lipid compositions. The membrane bending rigidity of SUVs increased with increasing chain length and saturation, resulting in differences in the vesicle rigidity and deformable capacity. Furthermore, we tested the tumor delivery capacity of liposomes with low, intermediate, and high rigidity as typical models for SUVs. Interestingly, liposomes with intermediate rigidity exhibited better tumor extracellular matrix diffusion and multicellular spheroid (MCS) penetration and retention than that of their stiffer or softer counterparts, contributing to improved tumor suppression. Stiff SUVs had superior cellular internalization capacity but intermediate tumor delivery efficacy. Stimulated emission depletion microscopy directly showed that the optimal formulation was able to transform to a rod-like shape in MCSs, which stimulated fast transport in tumor tissues. In contrast, stiff liposomes hardly deformed, whereas soft liposomes changed their shape irregularly, which slowed their MCS penetration. Our findings introduce special perspectives from which to map the detailed mechanical properties of SUVs with different compositions, provide clues for understanding the biological functions of SUVs, and suggest that liposome mechanics may be a design parameter for enhancing drug delivery.**

KEYWORDS: *SUVs, liposome, chain length and saturation, membrane mechanics, vesicle rigidity, ECM penetration, tumor delivery*

Small unilamellar vesicles (SUVs) enclosed by lipid bilayers are widespread in biological organisms. Typical examples of SUVs include exosomes, synaptic vesicles, and argosomes.[1,2] They play active roles in various biological functions, such as cell−cell communication, signaling, and cargo delivery. Many of these processes are facilitated by changes in the lipid properties, such as the length and saturation degree of the acyl chain, which influence the mechanical properties of the SUVs.[3−5] For instance, many deep-sea organisms contain high proportions of polyunsaturated fatty acids, which reduce the rigidity of SUVs and enable adaptation to the high-pressure environment.[6] The mechanical properties of SUVs also regulate the stability, size, shape, and penetration capacity of the vesicles.[7−9] However, the physical feedback mechanisms that

Received: February 12, 2019
Accepted: June 8, 2019
Published: June 8, 2019

DOI: 10.1021/acsnano.9b01181
ACS Nano 2019, 13, 7676−7689

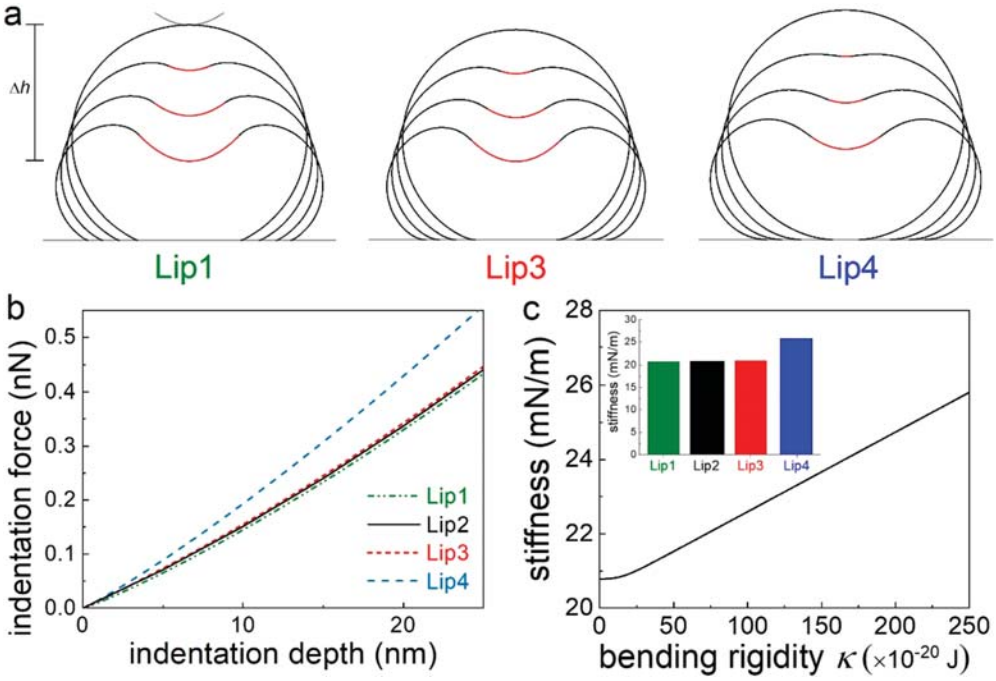

Figure 1. Theoretical modeling of vesicle indentation. (a) Equilibrium configurations of vesicles composed of Lip1, Lip3, and Lip4 at indentation depths Δh = 0, 30, 60, and 90 nm. The indenter tip has a parabolic shape (light gray curve). Red curves represent the regions of contact between the vesicles and indenter tips. Gray curves indicate the flat surfaces of the substrates. There is no adhesion between the indenter tip and the vesicle. (b) Corresponding indentation force−displacement curves. (c) Vesicle stiffness as a function of the membrane bending rigidity. Inset: theoretically calculated stiffnesses of vesicles Lip1, Lip2, Lip3, and Lip4.

underpin these lipid composition changes have not been systematically studied, which is crucial for both understanding biological functions[10−13] and developing effective drug delivery systems.

Recent investigations have revealed that vesicle rigidity governs cellular internalization, which further modulates circulation, biodistribution, and tissue targeting.[10,11] However, the mechanistic understanding of how vesicle rigidity alters cell uptake is still unclear.[12] Despite continuing studies on cell uptake, the details of the effects of vesicle rigidity on more detailed drug delivery processes, especially barrier penetration and targeting under flow, remain largely unexplored. In biological environments, visualizing the microscopic movement of vesicles requires high sensitivity and spatiotemporal resolution,[13] and exploring the micromotion mechanism of vesicles *in vitro* and *in vivo* is a challenging task. Therefore, vesicle rigidity, though analyzed and confirmed in our current study, is not yet recognized as a promising design parameter regulating drug delivery efficiency.

The mechanical properties of the lipid membrane depend on the lengths and saturation degrees of acyl chains, which further regulate the mechanical behaviors of the SUV as a whole structure.[3−5] Herein, we first developed a theoretical model to describe the mechanical response of SUVs with different lipid compositions in terms of the bending properties of the SUV membranes. Liposomes, artificial SUVs,[14,15] were then prepared to test this model and to explore the influence of the mechanical properties of SUVs on cancer therapy. Theoretical analysis uncovered a linear relationship between the indentation rigidity and the bending properties of the SUV membrane, which becomes less flexible as the lipid chain length increases; that is, the rigidity increases as the lipid saturation and chain length increase, which was confirmed by an atomic force microscopy (AFM)-based approach. We further explored the role of liposome rigidity in tumor extracellular matrix (ECM) diffusion, tumor penetration, and accumulation as well as *in vivo* distribution. Our results showed that liposomes with intermediate rigidity exhibited superior diffusion behaviors in the ECM and enhanced penetration in multicellular spheroids (MCSs) compared to their stiff or soft counterparts, contributing to longer retention in tumor sites and better tumor suppression in the animal model. We visualized the liposomes through stimulated emission depletion (STED) microscopy and found that the optimal formulation was able to transform to a rod-like shape in ECM, which stimulated their fast transport in tumor tissues.

RESULTS

Theoretical Modeling of Vesicle Indentation and Axisymmetric Compression. The composition of the lipids (*i.e.*, the acyl chain length and saturation) influences their phase state, which in turn affects the mechanical properties of SUVs.[16] Herein, we considered six different nanovesicles as typical models: Lip1, mainly composed of 1,2-dilauroyl-*sn*-glycero-3-phosphocholine (DLPC, C12:0); Lip2, mainly composed of 1,2-dimyristoyl-*sn*-glycero-3-phosphocholine (DMPC, C14:0); Lip3, mainly composed of 1,2-dipalmitoyl-*sn*-glycero-3-phosphocholine (DPPC, C16:0); Lip4, mainly composed of 1,2-distearoyl-*sn*-glycero-3-phosphocholine (DSPC, C18:0); Lip5, mainly composed of 1,2-dioleoyl-*sn*-glycero-3-phosphoethanolamine (DOPE, C18:1); and Lip6, mainly composed of 1,2-distearoyl-*sn*-glycero-3-phosphocholine (DEPC, C22:1). Based on the bending properties of the membranes composed of these six different kinds of lipids,[3,4] we performed theoretical analysis

DOI: 10.1021/acsnano.9b01181
ACS Nano 2019, 13, 7676−7689

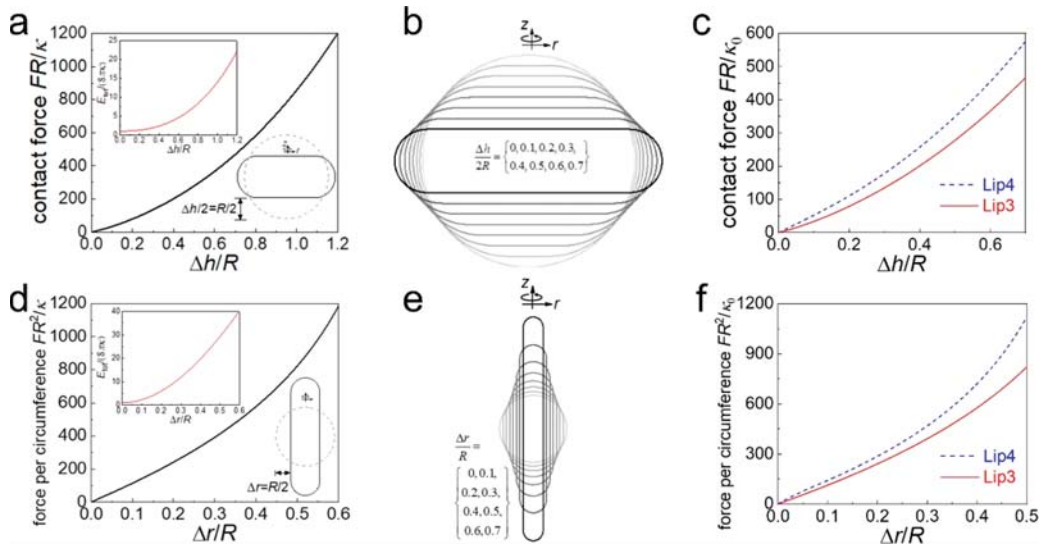

Figure 2. Vesicle deformation upon compression. (a–c) Vesicle compressed between two parallel rigid flat plates. (a) Normalized vertical contact force $F = dE_{tot}/d(\Delta h)$ as a function of the normalized change in the distance Δh between two parallel plates. Insets: total free energy E_{tot} as a function of Δh (top left); the initial vesicle shape (dashed line) and equilibrium vesicle configuration at $\Delta h = R$ (solid line) (bottom right). (b) Selected equilibrium configurations at different Δh. The parameters are $\kappa = 24 \times 10^{-20}$ J, $R = 75$ nm, and $\Delta p = 3 \times 10^5$ Pa, as in Figure 1a (Lip3). There is no adhesion between the vesicle and plates ($\gamma = 0$). (c) Force–displacement curves for vesicles considered in panel (a). (d–f) Vesicle confined in a rigid cylindrical tube undergoing radial shrinking. (d) Normalized force per contact circumference $F = dE_{tot}/d[\pi(R - \Delta r)^2]$ as a function of the normalized change in the radius Δr of the shrinking cylindrical tube. Insets: total free energy E_{tot} as a function of Δr (top left); the initial vesicle shape (dashed line) and equilibrium vesicle configuration at $\Delta r = R/2$ (solid line) (bottom right). (e) Selected equilibrium configurations at different Δr. (f) Force–displacement curves for vesicles in Figure 2d.

of the indentation of initially spherical vesicles with different membrane bending rigidities on an adhesive flat rigid substrate. Here, we adopted the Helfrich–Canham membrane theory to characterize the vesicle deformation and determined the equilibrium states of the vesicles upon indentation through numerical optimization.[17] Upon indentation, the lipid vesicles have the same fixed surface area, $4\pi R^2$, with an osmotic pressure, Δp, and are subjected to axisymmetric elastic deformation in cylindrical coordinates (r,ϕ,z). The total system energy is characterized by the Canham–Helfrich model as

$$E_{tot} = 2\pi\kappa \int_0^l r\left(\frac{d\psi}{ds} + \frac{\sin\psi}{r}\right)^2 ds - \Delta p(V - V_0) - \gamma A_c$$

where ψ, s, and κ are the tangent angle, arclength, and bending rigidity of the vesicle membrane; the arclength s of the free vesicle membrane starts from the edge of contact ($s = 0$) between the vesicle and the flat substrate and reaches $s = l$ at the north pole of the vesicle; Δp represents the pressure difference between the interior and exterior of the vesicle; $V = \pi\int_0^l r^2 \sin\psi\, ds$ and $V_0 = 4\pi R^3/3$ are the volume of the deformed and initial spherical vesicle, respectively; and γ (>0) is the adhesion energy and $A_c = \pi r_c^2$ is the surface area of the circular contact region of radius r_c. A zero spontaneous curvature is assumed. We have omitted the energy contribution associated with the Gaussian modulus of the vesicle membrane as it is constant due to the Gauss–Bonnet theorem and does not affect the vesicle deformation. The surface area of the vesicle is fixed at $2\pi\int_0^l r\,ds + A_c = 4\pi R^2$. With the geometric relations $dr/ds = \cos\psi$ and $dz/ds = \sin\psi$, the system energy E_{tot} can be expressed as a function of the tangent angle ψ, which is approximated by a cubic B-spline function as $\psi(s) = \sum a_i N_i(s)$ $(i = 0,...,m)$, where the control points a_i serve as the coefficients of the basic functions $N_i(s)$.[15]

To determine the minimum energy state of the vesicle at a certain indentation depth Δh, we employ the interior-point method in constrained nonlinear numerical optimization to minimize the total energy E_{tot} with respect to the control points a_i, where the fixed surface area of the vesicle serves as an equality constraint, and the prevention of the penetration of the vesicle by the indenter tip is expressed as an inequality constraint. Once the tangent angle $\psi(s)$ is known, the total energy and the corresponding vesicle shape at a certain Δh can be determined. The effective indentation force F is determined numerically from $F = dE_{tot}/d(\Delta h)$. Here, we assume that the tip has a parabolic shape with curvature $1/R_{tip}$ at its apex and take $R_{tip} = 30$ nm. The vesicle radius is taken to be $R = 75$ nm, as indicated in our experiments below, and the osmotic pressure $\Delta p = 3 \times 10^5$ Pa is adopted as reported in the study on the mechanical behaviors of nanovesicles.[2] The adhesion energy is $\gamma = 1.2$ mJ/m^2. The bending rigidity κ of the vesicle membrane composed of Lip1 (DLPC main) is taken to be 3×10^{-20} J, κ of Lip2 (DMPC main) is 15×10^{-20} J, κ of Lip3 (DPPC main) is 24×10^{-20} J, κ of Lip4 (DSPC main) is 250×10^{-20} J, κ of Lip5 (DOPE main) is 0.6×10^{-20} J, and κ of Lip6 (DEPC main) is 10×10^{-20} J.[3,4]

Figure 1a shows the shapes of Lip1, Lip3, and Lip4 vesicles at indentation depths $\Delta h = 0$, 30, 60, and 90 nm. The selected equilibrium configurations for Lip2, Lip5, and Lip6 vesicles are shown in Supporting Information Figure S1. As Δh increases, the region of contact between the substrate and vesicle also increases, and the vesicle evolves from an approximately spherical cap to a concave shape. The lower the bending rigidity κ is, the larger the vesicle–substrate contact region is (Figure 1a). With knowledge of the total system energy E_{tot} as a function of the indentation depth Δh, the indentation force $F = dE_{tot}/d(\Delta h)$ can be determined (Figure 1b), and the vesicle

DOI: 10.1021/acsnano.9b01181
ACS Nano 2019, 13, 7676–7689

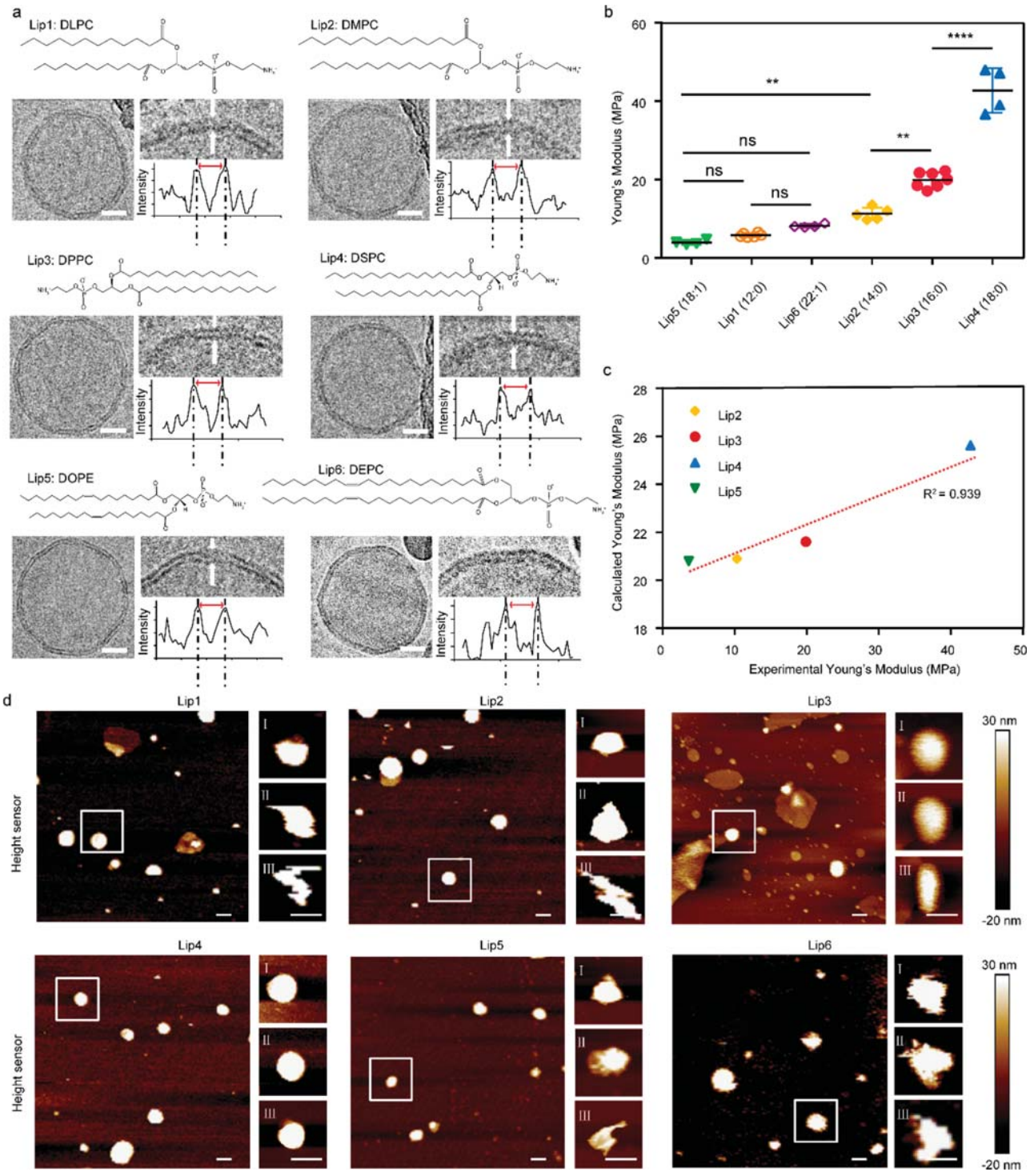

Figure 3. Characterizations of liposomes. (a) Cryogenic transmission electron microscopy (cryo-TEM) images of liposomes. The width of the phospholipid bilayer of each liposome is approximately 4 nm. Scale bar: 20 nm. (b) Young's modulus of liposomes tested by AFM in solution. (c) Correlation between the experimental Young's modulus data and the calculated Young's modulus values. (d) Corresponding deformation images of liposomes when acted on by external forces. I, 100 pN; II, 500 pN; and III, 1000 pN. Scale bar: 100 nm. Data are presented as the mean ± SD ($n \geq 5$). $P > 0.05$, ns; $^{**}P < 0.01$; $^{****}P < 0.0001$.

stiffness $dF/d(\Delta h)$, defined as the derivative of the applied indentation force with respect to the indentation depth, is adopted to characterize the vesicle rigidity (Figure 1c). A similar scheme is used in theoretical studies on the indentation of pore-spanning lipid membranes.[18] At the same Δh, a vesicle with a higher κ requires a higher indentation force F (Figure 1b). As shown in Figure 1a,b, the vesicle stiffness maintains a nearly constant value at relatively small κ. At relatively large κ (*e.g.*, $\kappa >$

DOI: 10.1021/acsnano.9b01181
ACS Nano 2019, 13, 7676−7689

25×10^{-20} J in our case studies), the vesicle stiffness is almost linearly proportional to κ (Figure 1b). These results revealed that liposomes formed from membranes with lower bending rigidity exhibit lower Young's modulus values and display more significant deformation upon indentation.

In addition to the vesicle indentation, we also performed theoretical analysis of the compression of a vesicle between two parallel rigid flat plates and confined in a shrinking rigid cylindrical tube (Figure 2). We assume that the compressed vesicle undergoes axisymmetric deformation, and that there is no adhesion between the vesicle and the plates or the tube wall. As shown in Figure 2a, the contact force $F = dE_{tot}/d(\Delta h)$ applied to the vesicle increases as Δh increases, where Δh represents the change in the distance between two parallel plates. The profile of the corresponding total free energy E_{tot} is shown in the top right inset in Figure 2a. The vesicle shapes at $\Delta h = 0$ and R are shown in the bottom right inset in Figure 2a. More selected equilibrium vesicle shapes at different Δh are shown in Figure 2b. To investigate the effect of the bending rigidity κ on the contact force, we perform additional calculations at $\kappa = 250 \times 10^{-20}$ J (Lip4) and compare the obtained force profile $F(\Delta h)$ with that of Lip3 (Figure 2c). Here, $\kappa_0 = 24 \times 10^{-20}$ J (Lip3). At a given Δh, a vesicle with a higher κ experiences a larger contact force, as expected.

In the case of the radial compression of a vesicle confined in a shrinking rigid cylindrical tube, as shown in Figure 2d, the force per contact circumference $F = dE_{tot}/d[\pi(R - \Delta r)^2]$ increases as Δr increases, where Δr represents the change in the radius of the shrinking cylindrical tube. The total free energy profile and selected equilibrium vesicle shapes at different Δh are also presented in Figure 2d,e. The numerical results in Figure 2f indicate that a vesicle with higher κ (Lip4) experiences a larger force per contact circumference than a vesicle with lower κ (Lip3).

These results indicate that a vesicle with a membrane of a higher bending rigidity is much stiffer, and similar results are observed in the case of vesicle indentation. These two cases in Figure 2 may serve as approximations of vesicle transportation through the gap between two adjacent biological layers and within thin tunnels embedded in the tumor ECM. Here, we focus on the case of rigid confinements in our theoretical analysis and ignore the effect of confinement elasticity on the mechanical behaviors of vesicles. A thorough and sound theoretical determination of the mechanical interplay between vesicles and soft environments is challenging and deserves further detailed investigations in the future.

Experimental Observations Validate Mechanical Model Predictions. To test the mechanical model predictions and reveal their implications for the cell response and tumor delivery capacity of liposomes, we first prepared six different groups of liposomes and probed their mechanical properties. Previous studies have reported that nanoparticles (NPs) exhibit an obvious size effect against stiff pancreatic cancers;[19,20] herein, liposomes with a hydrodynamic diameter of approximately 85 nm were prepared (Figure 3a and Supporting Information Figure S2a), and the average thickness of the phospholipid bilayers of these liposomes was approximately 4 nm. The zeta-potential of all the liposomes was slightly negatively charged to ensure the same surface charge (Supporting Information Table S1). The stability of the prepared liposomes was confirmed in fetal bovine serum (FBS) (Supporting Information Figure S2b,c). For drug delivery, hydroxycamptothecin (HCPT), an anticancer drug, was then encapsulated in liposomes. The entrapment efficiency (EE%) was nearly the same in all liposome preparations (Supporting Information Table S1). Furthermore, the *in vitro* release of HCPT from all six liposome formulations was found to be sustained up to 24 h at pH 7.4 and 6.0 (Supporting Information Figure S2d,e).

We then used AFM-based indentation to evaluate the rigidity of liposomes in solution. For liposomes composed of saturated lipids, the Young's modulus increased gradually with lipid chain length; that is, the vesicle rigidity increased from Lip1 to Lip4 (Figure 3b). However, for liposomes composed of unsaturated lipids, even lipids with long chain length but one degree of unsaturation, the vesicle rigidity decreased dramatically with lipid unsaturation. The Young's modulus of Lip3 (19.9 MPa) was approximately 3.4 times Lip1 (5.8 MPa) and 0.46 times Lip4 (42.8 MPa) (Figure 3c). There was no significant difference in the Young's modulus among Lip1, Lip5, and Lip6 (Figure 3c). We note that the measured values of the Young's modulus showed good correlation with the calculated results (Figure 3c). Furthermore, these liposomes were analyzed by AFM-based mechanical mapping. The liposomes were originally ball shaped; as the applied force added (from 100 pN to 1 nN), however, the liposomes eventually deformed into various shapes depending upon the magnitude of the forces and the rigidity of the liposomes (Figure 3d and Supporting Information Figure S3). Lip1, Lip2, Lip5, and Lip6 deformed irregularly, whereas Lip3 changed from spherical to ellipsoidal shape. However, only mild deformation was observed for Lip4. These results were consistent with our theoretical modeling, showing that the rigidity of nanovesicles increases with increasing lipid chain length and saturation.

***In Vitro* Modeling of Extracellular Matrix Permeation.** We further explored the delivery efficacy of synthesized liposomes for tumor therapy to evaluate how the mechanical properties of SUVs affect their biological behaviors. The tumor ECM, which consists of fibrous proteins forming a cross-linked gel-like structure, dramatically hinders the permeation of therapeutics into tumor cells through size filtering and electrostatic interaction.[21,22] We used multiparticle tracking (MPT) to explore the movement of liposomes in the simulated tumor ECM. The ensemble-averaged geometric mean-squared displacement ($\langle MSD \rangle$) value of Lip3 was significantly higher than those of Lip1, Lip2, Lip4, Lip5, and Lip6 (Figure 4a–c). At the time scale of 1 s, Lip3 was approximately 11.8, 5.2, and 4.1 times the $\langle MSD \rangle$ value of Lip5, Lip2, and Lip4, respectively (Figure 4d).

***In Vitro* Cellular Uptake Studies.** The impact of SUV mechanics on cellular uptake *in vitro* was then examined in two different cell lines: pancreatic adenocarcinoma cells (BxPC-3) and human pancreatic stellate cells (HPSC). The cellular uptake pattern of these two cell lines was similar to that described in previous reports;[23–25] that is, the more stiff the liposome was, the greater the cellular uptake was. Lip4 was internalized to a greater extent than the rest of the liposomes. We note that Lip1, Lip5, and Lip6 displayed no significant difference in cellular uptake (Figure 5a), which might result from their similar physicochemical properties, including size, surface charge, and rigidity. The quantitative results were consistent with the qualitative analysis (Figure 5b). In addition, we analyzed the *in vitro* cytotoxicity of different liposomes by a 3-(4,5-dimethylthiazol-2-yl)-2,5-diphenyltetrazolium bromide (MTT) assay. All liposomal formulations were confirmed to be nontoxic at the tested concentrations (Supporting Information Figure S4). The half-maximal inhibitory concentration (IC_{50}) of HCPT-loaded

DOI: 10.1021/acsnano.9b01181
ACS Nano 2019, 13, 7676–7689

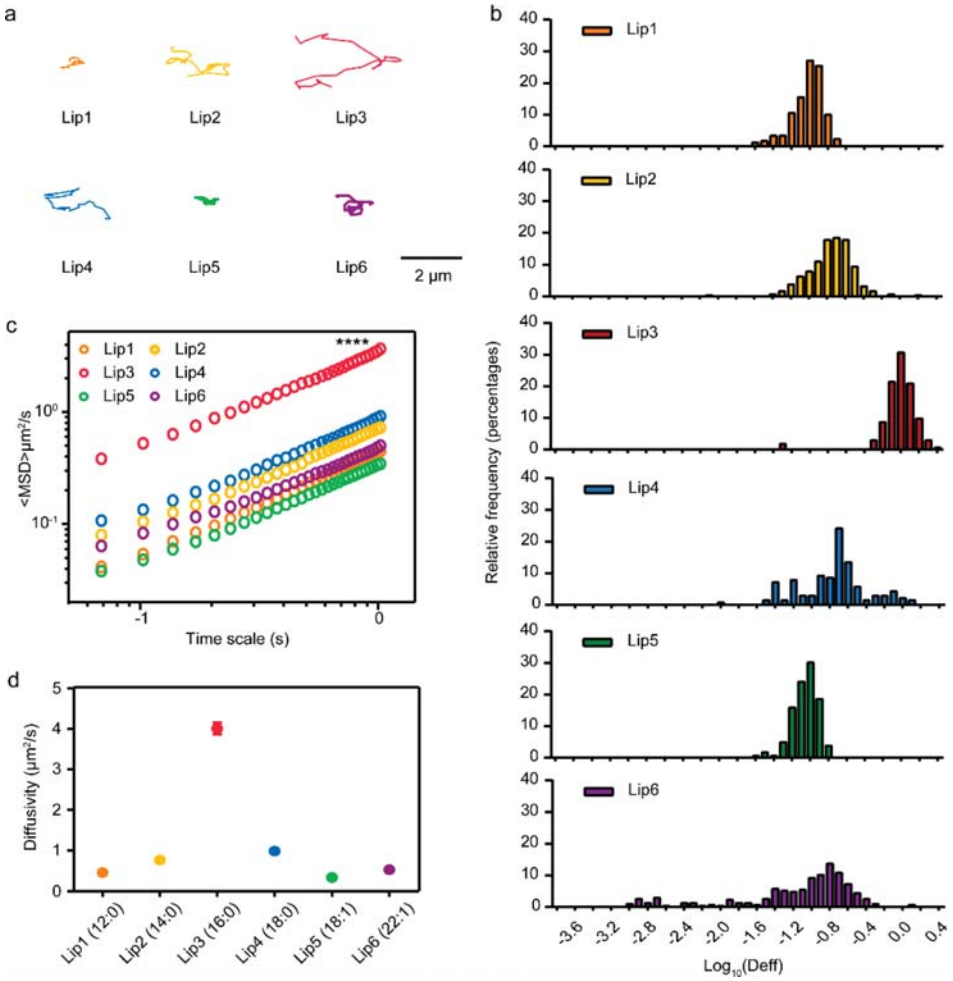

Figure 4. Diffusion of liposomes *in vitro*. (a) Representative trajectories of liposome diffusion in simulated ECM in 1 s. (b) Distributions of the logarithms of individual liposome effective diffusivity (D_{eff}) values in simulated ECM at 1 s. (c) ⟨MSD⟩ values for liposomes in simulated ECM in 1 s. (d) Diffusivity of liposomes at 1 s in simulated ECM; $n = 300$; ****$P < 0.0001$.

liposomes was also calculated (Figure 5c,d), and the Lip4 liposomes had the lowest IC_{50} compared to that of the rest of the liposomes in the two cell lines, which might result from their efficient cell internalization. Thus, these results revealed that rigid SUVs were more readily internalized by cells than their soft counterparts.

To explore how these liposomes were internalized, we utilized three different endocytosis inhibitors (chlorpromazine (CPZ) for the inhibition of clathrin-mediated endocytosis, filipin for the inhibition of caveolae-mediated endocytosis, and dynasore for the inhibition of both clathrin- and caveolae-mediated endocytosis). As can be seen in Supporting Information Figure S5, both BxPC-3 and HPSC cells treated with CPZ showed reduced uptake of all liposomes (Lip1−Lip6), indicating that all liposomes were internalized through clathrin-mediated endocytosis. In addition, recent studies using simulations and computational methods have indicated that hard NPs are internalized smoothly by cells, whereas soft NPs undergo deformation, which requires larger adhesion energies to complete membrane wrapping.[25−27] This higher energy requirement may partly explain why liposomes of relatively lower stiffnesses undergo relatively difficult cellular uptake.

Penetration of Liposomes in Multicellular Spheroids.

Due to the similarity in morphology and biological microenvironment to solid tumors, MCSs are widely used for screening cancer therapeutics.[28,29] Recently, reports have shown that many solid tumors, such as breast cancer, prostate cancer, ovarian cancer, and particularly pancreatic cancer, are similar in exhibiting stromal fibrosis; in pancreatic cancer fibrosis, the fibrous matrix accounts for more than 90% of the total tumor volume.[30] To biologically mimic solid tumors full of ECM, HPSC cells, which can secrete a large number of fibers and are the main source of pancreatic fibrosis in the stroma, were cocultured with BxPC-3 cells to form BxPC-3-HPSC MCSs. In normal humans, HPSC cells have two phenotypes, that is, static and activated.[31,32] When HPSC cells are activated, they secrete a large amount of fibrin, and α-smooth muscle actin is a marker of activation.[33] We then used the α-smooth muscle actin (α-SMA) antibody to check the phenotype of HPSC.[34−36] The BxPC-HPSC MCSs showed apparent green fluorescence distribution and protein expression, indicating that the HPSC cells were in the active state and producing large amounts of ECM proteins, whereas little ECM could be observed in BxPC MCSs (Figure 5e). The penetration ability of liposomes was then quantitatively and qualitatively monitored by confocal laser scanning

DOI: 10.1021/acsnano.9b01181
ACS Nano 2019, 13, 7676−7689

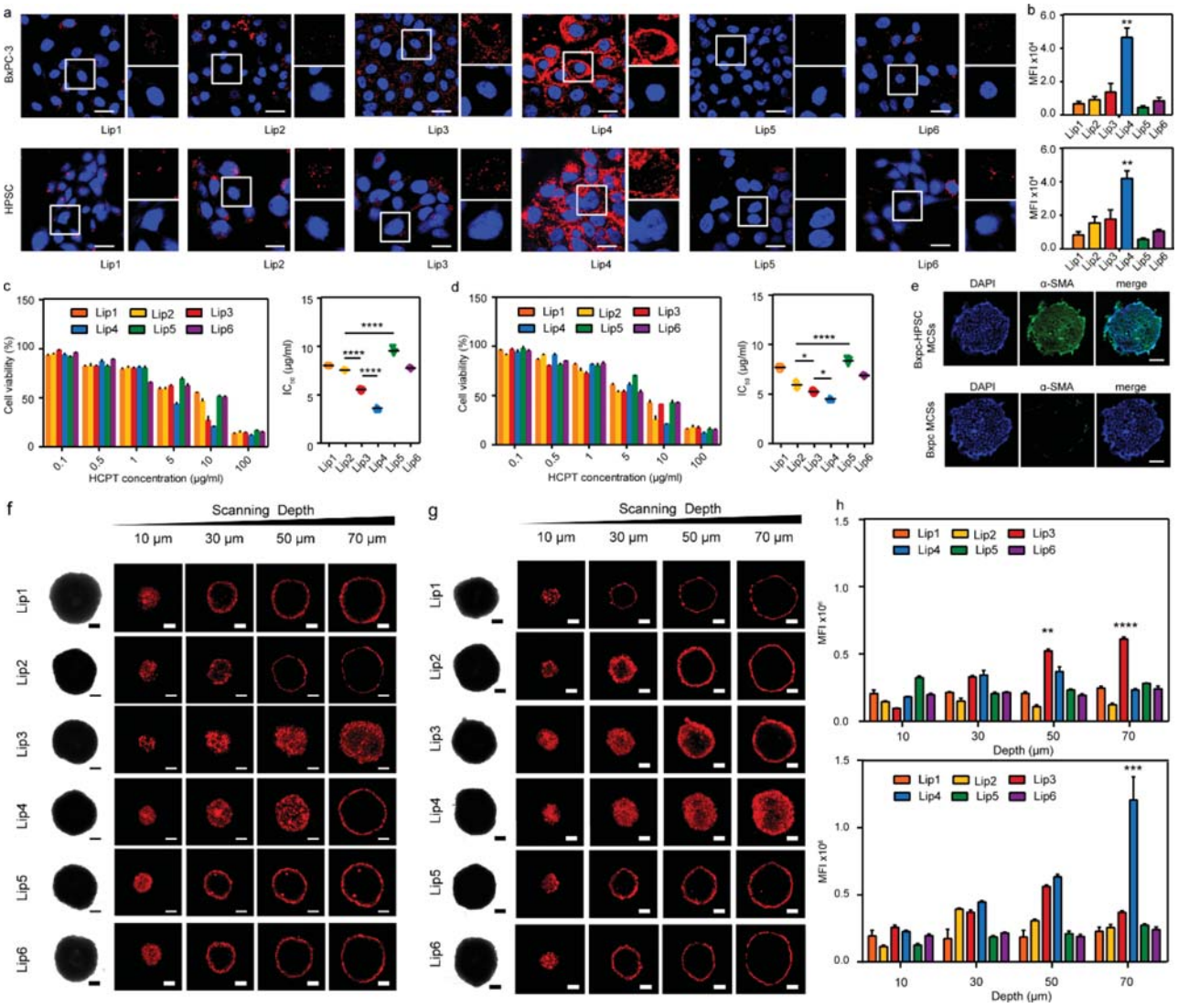

Figure 5. Cellular internalization and MCS penetration. (a) Confocal laser scanning microscopy (CLSM) images of the cellular uptake of liposomes in BxPC-3 and HPSC cells. Blue, nuclei stained with 4′,6-diamidino-2-phenylindole (DAPI). Red, DiI-labeled liposomes. Scale bars: 50 μm. (b) Mean fluorescence intensity of liposomes in BxPC-3 cells (top) and HPSC cells (bottom) detected by BCA. (c,d) Cell viability and IC_{50} values in BxPC-3 and HPSC cells, respectively. (e) Immunofluorescent staining of α-SMA in BxPC-3-HPSC MCSs and BxPC-3 MCSs using the α-SMA antibody and observed under a confocal microscope. Scale bar: 100 μm. (f,g) *In vitro* penetration of DiI-labeled liposomes (red) in BxPC-3-HPSC MCSs and BxPC-3 MCSs. MCSs were incubated with different liposomes and imaged by CLSM *Z*-stack scanning after 2 h. The MCS surface was settled at 0 μm. Scale bar: 50 μm. (h) Quantification of the depth of liposome penetration in BxPC-3-HPSC MCSs (top) and BxPC-3 MCSs (bottom). The data are shown as the means ± SD (n = 5). *P < 0.05, **P < 0.01, ***P < 0.001, ****P < 0.0001.

microscopy (CLSM) (Figure 5f–h). Surprisingly, Lip3 displayed the best penetration at all scanning depths, and more Lip3 than the rest liposomes diffused into the MCSs. We surmise that because Lip3 could more easily penetrate the ECM around the tumor cell, more Lip3 penetrated the BxPC-3-HPSC MCSs and then entered tumor cells. Lip1, Lip2, Lip5, and Lip6 displayed lower penetration due to their low diffusivity and weak cellular uptake. In contrast, Lip4 exhibited moderate penetration, mainly resulting from its moderate diffusivity. We also constructed MCSs with only BxPC-3 cells, which lacked ECM (Figure 5g). In contrast, the penetration of Lip4 in BxPC-3 MCSs was higher than that of the rest of the liposomes, which was consistent with a previous report showing that tumor cells uptake hard particles more readily than soft particles.[37,38]

***In Vivo* Animal Imaging and Tumor Penetration.** Lip1, Lip5, and Lip6 showed similar ECM diffusion, cellular uptake, and MCS penetration capacity *in vitro* and *ex vivo*, indicating that they might have similar *in vivo* behaviors. Thus, Lip5 was then used as the representative vesicle for Lip1 and Lip6 in the following experiments; Lip2, Lip3, Lip4, and Lip5 were tested for the *in vivo* studies. To evaluate the impacts of SUV mechanics on their *in vivo* tissue penetration, IR783-labeled liposomes were peritumorally injected into BxPC3-HPSC-bearing nude mice. As shown in Figure 6a,d, the fluorescence intensity of these four liposomes decreased over time, and they showed similar fluorescence intensity postinjection. However, the rate of fluorescence intensity reduction varied greatly among these three liposomes. The fluorescence intensity of Lip2, Lip4, and Lip5 decreased quickly, but the fluorescence intensity of Lip3

DOI: 10.1021/acsnano.9b01181
ACS Nano 2019, 13, 7676–7689

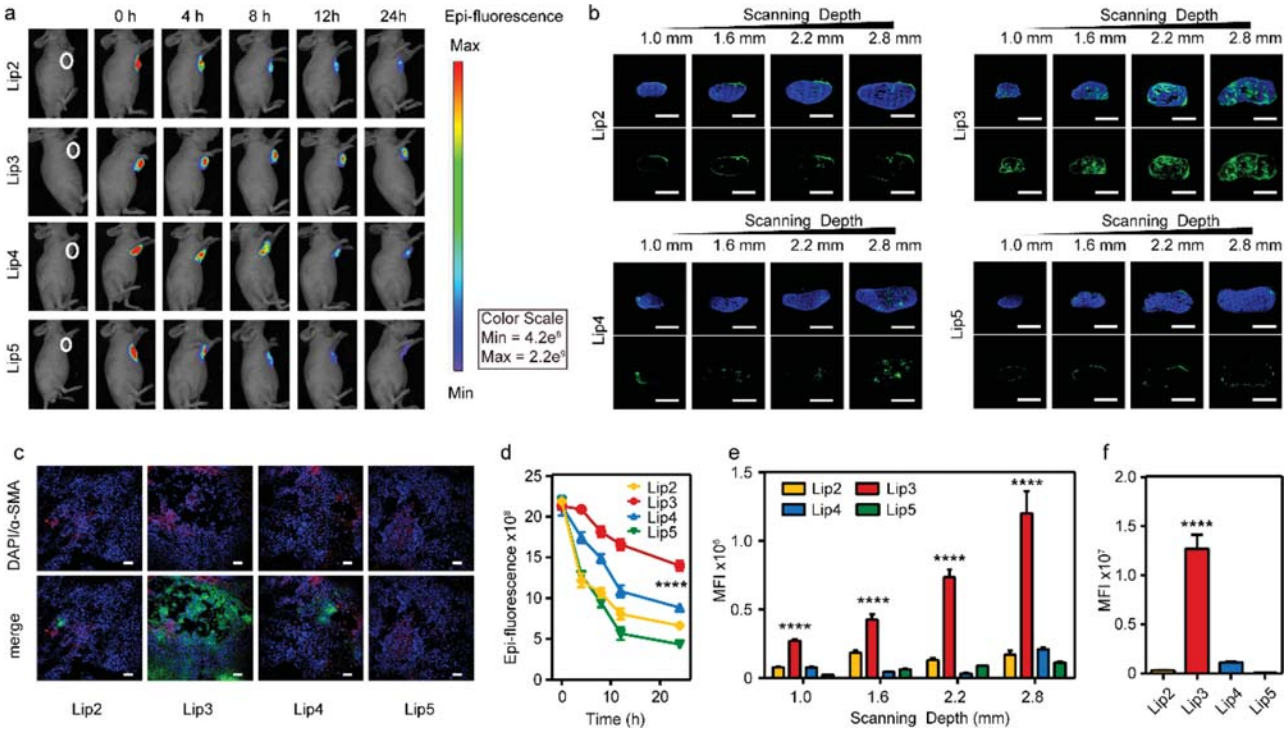

Figure 6. ***In vivo*** **tumor penetration. (a) Representative living images of nude mice bearing BxPC-3-HPSC tumor after peritumoral injection with different liposomes labeled with IR783 (40 μg/mL) (n = 5). (b) Representative images show the distribution of DSPE-PEG2000-FITC-labeled liposome (green) in BxPC-3-HPSC tumors. The tumors were sliced and imaged with a 10× objective. The nuclei were stained with DAPI (blue). Scale bar: 5 mm (n = 5). (c) Immunofluorescence staining images of the intratumor distribution of liposomes 2 h after a single injection. Liposomes were tagged with DSPE-PEG2000-FITC (green); ECM was labeled with α-SMA antibody (red) and cell nuclei were stained with DAPI (blue). Scale bars, 200 μm (n = 5). (d) Quantitative analysis of *in vivo* imaging at the tumor site of each group (n = 5). (e) Quantification of the distribution of liposome penetration in tumor tissues at different scanning depth (n = 5). (f) Quantitative analysis of the intratumor distribution of liposomes (n = 5). All data are presented as the mean ± SD (n = 5). ****P < 0.0001.**

decreased gradually, and 63% of Lip3 remained in the tumor at 24 h, which was approximately 3.3, 2.1, and 1.5 times the remaining amounts of Lip1, Lip2, and Lip4, respectively. The penetration ability of DSPE-PEG2000-FITC-labeled liposomes was then quantitatively and qualitatively monitored by CLSM (Figure 6b,e). For Lip3, we found a gradient of green fluorescence from the tumor edge to the core (Figure 6b). Lip4 showed only a few green signals at the tumor core. Lip2 and Lip5 exhibited fluorescence only at the edge of tumor tissue. At the scanning depth of 2.8 mm, the fluorescence intensity of Lip3 was approximately 4.8, 6.2, and 8.8 for Lip4, Lip2, and Lip5, respectively (Figure 6e). These results suggested that Lip3 was more effectively internalized into tumor tissues and maintained at the tumor sites. The significantly enhanced tumor accumulation of Lip3 could be attributed to their superior ECM diffusivity. To verify this hypothesis, we visualized the intratumoral distribution of DSPE-PEG2000-FITC-labeled liposomes by immunofluorescence staining (Figure 6c,f). Lip3 distributed widely throughout the tumor tissue, indicating their effective penetrating capability. In contrast, Lip2, Lip4, and Lip5 were unable to penetrate deep into the entire tumor tissue. Similar results could be found for liposomes labeled with DiI (Supporting Information Figures S7 and S8). These results demonstrated that Lip3 penetrated more easily into the tumor interstitial space and thus showed extraordinary enhanced tumor deposition in the entire tumor tissue.

Antitumor Activity Study in BXPC-3-HPSC Tumor Xenografts. We then evaluated the antitumor effect of HCPT-loaded liposomes in mice bearing BxPC-3-HPSC tumor xenografts. It is shown in Figure 7a that all of the formulations caused negligible change in body weight throughout the treatment periods, implying good biocompatibility of all the tested liposomes. The tumor volume was measured (Figure 7b), and tumors were weighed and imaged at the end of the study (Figure 7c,d). The Lip1 group showed an antitumor efficiency better than that of the phosphate-buffered saline (PBS) control. The control group displayed an antitumor efficiency slightly better than that of the Lip1 group, which could be explained by the increased ECM penetration (Supporting Information Table S1). The Lip3 group exhibited the strongest tumor inhibitory effect, mainly due to its efficient ECM penetration and excellent cellular uptake abilities. The Lip3 group exhibited clear DNA damage and membrane lysis (Figure 7e), implying that HCPT-loaded Lip3 produced significant tumor cell apoptosis. The extent of apoptosis decreased in the Lip4, Lip2, control, and Lip5 groups. No apoptosis was found in the blank group, as confirmed by TUNEL staining. Therefore, the improved penetration and cellular uptake capacities of liposomes with intermediate rigidity can enhance the efficacy of chemotherapy.

Observing the Movement and Transformation of Liposomes in the Tumor ECM. To better understand the mechanisms of liposome penetration into the tumor tissue, scanning electron microscopy (SEM) was used to analyze the tumor tissue microstructures: tumor cells and ECM (Figure 8a), ECM (tumor tissue after trypsin incubation) (Figure 8b), and

DOI: 10.1021/acsnano.9b01181
ACS Nano 2019, 13, 7676−7689

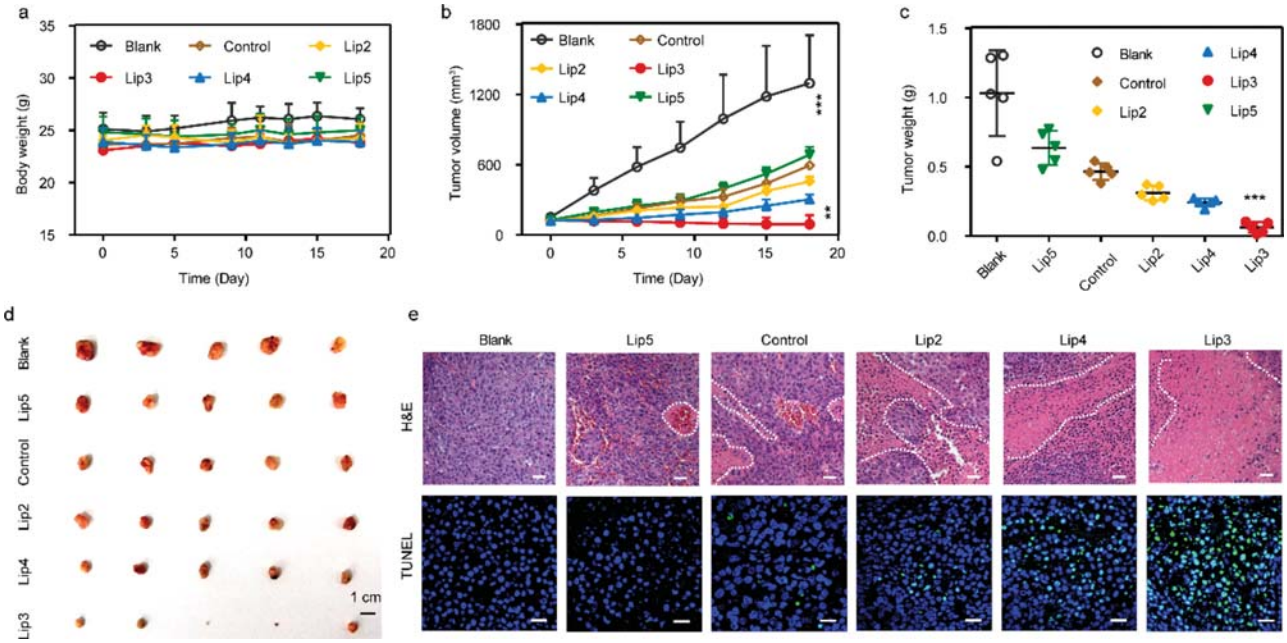

Figure 7. ***In vivo*** **tumor growth inhibition study in BxPC-3-HPSC tumor xenografts. When the tumor volume reached 100 mm^3, the tumor-bearing mice were randomly grouped and then injected with HCPT-loaded liposomes, control, or PBS. (a) Body weight of nude mice bearing BxPC-3-HPSC tumors during different formulation treatments. Blank: PBS. (b) Tumor volumes with varying treatments. (c) Weight of BxPC-3-HPSC tumors at the end of the treatment. (d) Photographs of the tumors taken at the end of the antitumor studies. Tumor-bearing nude mice were administered liposomal formulations for 3 weeks. (e) H&E staining (top row) and TUNEL immunohistochemical staining (bottom row) of tumor sections. The green signals represented the apoptotic and necrotic cells. Scale bars, 50 μm. Data are presented as the mean $\pm$ SD (n = 5). $^{**}P < 0.01$, $^{***}P < 0.001$ (n = 5).**

simulated tumor ECM (Supporting Information Figure S6). All the ECM had a fibrous network structure and a similar pore size, which implied that the liposome would undergo transformation within these fibrous structures. We then applied high-speed super-resolution imaging to visualize the movement of vesicles in MCSs directly. As it can be seen in Figure 8c and the Supporting Information (Movies S1, S2, S3, and S4), Lip1, Lip2, and Lip5 in the tumor stroma were deformed irregularly and diffused in a small area. Lip3 changed from spherical to ellipsoidal with high-speed movement. In contrast, Lip4 displayed little deformation during movement.

Previously, we have presented evidence that cylindrical/ellipsoidal NPs exhibit diffusion capacity that is better than that of spherical NPs in biological hydrogels, such as the intestinal mucus and ECM.[39,40] Molecular simulations and stimulated emission depletion (STED) microscopy uncovered that the rotation of ellipsoid NPs in mesh medium contributes to the superior diffusion capacity. Therefore, once liposomes (Lip3) deformed into ellipsoids due to their moderate rigidity, and this thin shape could further facilitate their ECM diffusion. Soft liposomes (Lip2 and Lip5) were apt to undergo deformation due to their low rigidity, and the contact area between the liposomes and ECM could increase after deformation, resulting in increased adhesion. As a result, the soft liposomes exhibited the lowest diffusivity. In contrast, rigid liposomes (Lip5) could not deform and showed a moderate ECM diffusion capacity.

In addition, we calculated the aspect ratios (ARs) of liposomes during their diffusion process (Figure 8d). The ARs of Lip2 and Lip5 ranged from 0.8 to 4.0, indicating their excessive and irregular deformation pattern. The mean AR of Lip3 was approximately 2.5, suggesting that most of the Lip3 transformed into ellipsoids, which is consistent with our previous findings that there exists an optimal AR (approximately 3) for the maximum transport rate of rod-like NPs in adhesive hydrogel.[41] However, the AR of Lip4 was mainly 1.0, which meant that the majority of Lip4 remained spherical. During the entire movement, the rigidity of liposomes affected the deformation of the particles, determining the trajectory and speed of diffusion in the ECM.

CONCLUSIONS

Cells synthesize thousands of distinct lipids, most of which vary in acyl chain length and saturation. However, the function of many of these lipid variations is still uncertain. In this study, by using theoretical studies, together with *in vitro*, *ex vivo*, and *in vivo* experiments, we investigated how lipid composition affects the mechanical properties and drug delivery efficacy of SUVs. We demonstrated that the membrane bending rigidity increased as the acyl chain length and saturation increased, which contributed to differences in vesicle rigidity and deformation capacities.

It is interesting to note that the penetration patterns of liposomes in BxPC-3 and BxPC-3-HPSC MCSs were different. This discrepancy was mainly caused by the different inner structures of MCSs. BxPC-HPSC MCSs were full of ECM, whereas little ECM could be observed in BxPC MCSs. Therefore, the penetration of liposomes in BxPC MCSs was determined by cellular uptake capacity, whereas the penetration of liposomes in BxPC-HPSC MCSs was determined by ECM diffusion and cellular uptake capacity. As a result, liposomes with moderate rigidity showed low diffusion in BxPC-3 MCSs, which was consistent with previous results showing that the efficiency of penetration into single cancer cell MCSs increased with the liposome bending modulus.[38] In the BxPC-HPSC MCSs, due to

DOI: 10.1021/acsnano.9b01181
ACS Nano 2019, 13, 7676−7689

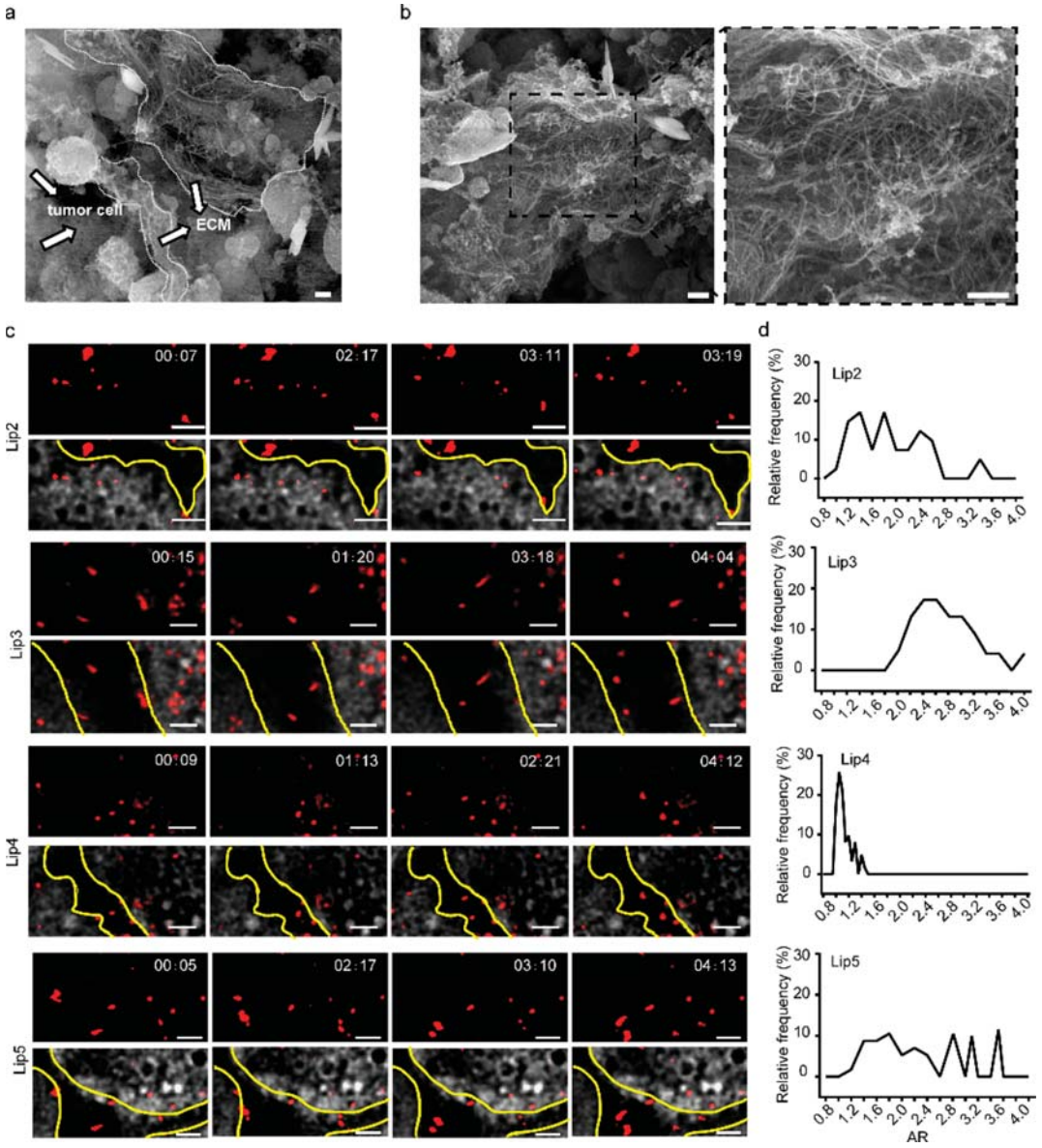

Figure 8. Observing the transportation of liposomes in the tumor ECM. (a) SEM images of tumor tissue stripped from mice bearing BxPC-3-HPSC xenograft tumors. Scale bars, 2 μm. (b) Tumor cell and ECM. (c) Snapshots and trajectories of liposomes in BxPC-3-HPSC MCSs, as imaged by stimulated emission depletion (STED) microscopy. STED microscopy images showing *in vitro* liposome deformation and movement in BxPC-3-HPSC MCSs. Scale bars, 1 μm. (d) Distribution of ARs for liposomes in (c). These data are calculated using ImageJ software (n = 100).

the fibrous network of ECM, liposomes with moderate rigidity deformed into ellipsoids during movement in the mesh structure, facilitating their ECM diffusion and thereby contributing to their cellular uptake and superior tumor penetration to that of other liposomes.

A recent study suggested that the intracellular uptake decreased with increase in the rigidity of NPs,[12] which is in sharp contrast to the observation in the present study. There are several potential factors that may explain the discrepancy observed in these two independent studies. First, almost all the physicochemical properties of the NPs in the referred work and our study are different, and these factors could result in the major discrepancies between our findings and their findings. Second, the elastic moduli are not within the same orders of magnitude, which might contribute to the different cellular uptake mechanism. Moreover, the cell lines used in our studies are not the same as these in the referred work.

By exploring how bending properties affect vesicle tumor delivery, we gained insight into the gatekeeping function of the ECM. Stiff vesicles had superior cellular internalization capacity but exhibited intermediate tumor delivery efficacy. On the other hand, vesicles of intermediate rigidity were the most effective formulation for tumor therapy compared to their soft and stiff counterparts, mainly due to their efficient ECM penetration ability. Thus, the ECM is the main barrier to the tumor delivery of the vesicles tested here. We anticipate that these results could inspire more research on designing strategies of overcoming the ECM barriers for ECM-rich tumors.

DOI: 10.1021/acsnano.9b01181
ACS Nano 2019, 13, 7676−7689

Despite a few successful liposomal pharmaceutical products in the 1990s, such as Doxil, Myocet, and AmBisome, the translational development of liposomal formulations for tumor delivery in clinical studies has been slow. It is now well-recognized that the success of liposome-based chemotherapy is significantly hampered by sequential drug delivery barriers, including tumor penetration and cellular internalization.[42] Here, we revealed that liposome rigidity plays important roles in drug delivery, and liposomes with intermediate rigidity exhibited better pancreatic tumor delivery than their soft and stiff counterparts. In addition, we note that elastic liposomes (Transfersome) could improve drug delivery into and through the skin.[43,44] From a practical perspective, our findings on the effects of the mechanical properties of liposomes on tumor delivery are of immediate interest for the rational design of vesicles for drug delivery.

In summary, we demonstrated that the chain length and saturation of lipids regulated the mechanical properties of SUVs, which further affected their biological behaviors, specifically tissue penetration by deformation-tuned diffusion across the ECM and cellular barriers. Three physically distinct liposomes that differed in lipid composition were prepared as typical models of SUVs. The membrane rigidity of SUVs increased with increasing acyl chain length and saturation, contributing to different vesicle rigidities and distinct deformation patterns, which directly regulated ECM penetration and tumor delivery. Taken together, our results provide critical insights into the role of biomechanical cues between the lipid composition and SUV mechanical properties, SUV and ECM, SUV and cell, and SUV and organ. This work assists the understanding of the mechanics of lipid vesicles and may guide the rational design of efficient liposome delivery systems.

METHODS

Materials. 1,2-Dioleoyl-*sn*-glycero-3-phosphoethanolamine (DOPE) and 1,2-dimyristoyl-*sn*-glycero-3-phosphocholine (DMPC) were purchased from Lipoid (Germany). 1-Palmitoyl-2-stearoyl-*sn*-glycero-3-phosphocholine (HSPC), 1,2-distearoyl-*sn*-glycero-3-phosphocholine (DSPC), 1,2-dihexadecanoyl-rac-glycero-3-phosphocholine (DPPC), 1,2-distearoyl-*sn*-glycero-3-phosphoethanolamine-*N*-[methoxy(polyethylene glycol)-2000] (DSPE-PEG2000), 1,2-dilauroyl-*sn*-glycero-3-phosphocholine (DLPC), 1,2-dierucoyl-*sn*-glycero-3-phosphocholine (DEPC), 1,2-distearoyl-*sn*-glycero-3-phosphoethanolamine-*N*-[(polyethylene glycol)-2000)]-fluorescein isothiocyanate (DSPE-PEG2000-FITC), and 1,2-distearoyl-*sn*-glycero-3-phosphoethanolamine-*N* [biotinyl (polyethylene glycol) 2000)] (ammonium salt) (DSPE-PEG2000-Biotin) were purchased from AVT Corporation (Shanghai, China). 1,2-Dioleoyl-*sn*-glycero-3-phosphoethanolamine-[methoxy(polyethylene glycol) 2000] (DOPE-PEG2000) was purchased from Avanti (USA). α-SMA and secondary Alexa Fluor 488-conjugated goat anti-rabbit IgG (H+L) were purchased from Abcam (Cambridge, UK). Hydroxycamptothecin (HCPT) was purchased from J&K China Chemical Ltd. 2-(4-Amidinophenyl)-1*H*-indole-6-carboxamidine (DAPI), secondary Alexa Fluor 555-conjugated donkey anti-rabbit IgG (H+L), and 1,1′-dioctadecyl-3,3,3′,3′-tetramethylindocarbocyanine perchlorate (DiI) were purchased from Beyotime BioTechnology (China). Filipin and dynasore were purchased from Dalian Meilun Biotechnology Co., Ltd. Chloroform, cholesterol, and glycerin were purchased from Sinopharm Chemical Reagent Co., Ltd. (Shanghai, China). Other reagents were of analytical grade.

Cell and Animal Care. A pancreatic adenocarcinoma cell line (BxPC-3) from the Chinese Academy of Sciences Shanghai cell bank was cultured at 37 °C and 5% CO_2 in Roswell Park Memorial Institute (RPMI) 1640 complete medium containing 10% serum. Human pancreatic stellate cells (HPSCs) from the United States Science Cell Research Laboratories were cultured at 37 °C and 5% CO_2 in Dulbecco's modified Eagle medium (DMEM) supplemented with 10% serum. Balb/c-nu/nu rats (20 g ± 5 g) were provided by the Animal Experiments Center of the Shanghai Institute of Materia Medica, Shanghai, China. Animals had free access to food and water. All animal procedures performed in this study were approved by the Animal Ethics Committee of Shanghai Institute of Materia Medica, Chinese Academy of Sciences (IACUC certification numbers 2017-08-GY-32 and 2018-01-GY-35).

Liposome Preparation and Characterization. Liposomes were prepared by a modified thin lipid film hydration method. Briefly, phospholipids and HCPT were dissolved in methanol and chloroform (1:3, v/v) in a round-bottom flask. The organic solvent was evaporated to form a homogeneous lipid film. Then, the lipid film was hydrated, followed by extrusion by using a mini-extruder (Avanti Polar Lipids). The liposome size and zeta-potential were measured by a NanoZS (Malvern). The encapsulation efficacy was detected by high-performance liquid chromatography (HPLC, Agilent).

Cryogenic Transmission Electron Microscopy (cryo-TEM). Cryo-TEM was adopted to visualize the structures of liposomes. Liposome suspension (200 μL) was dropped on a carbon-coated copper grid, blotted, and immersed in liquid ethane for shock-frozen product. The samples were then imaged by using a Tecnai 12 electron microscope at 200 kV.

Atomic Force Microscopy. The Bio-FastScan scanning probe microscope (Bruker) in PeakForce QNM imaging mode was used for AFM analysis. All the liposomes were detected in solution. In brief, we chose biotin-DSPE-PEG2000 to replace DSPE-PEG2000 for the liposome preparation, and the liposomes were hydrated in 10 mM $MgCl_2$ solution for 30 min. For liposome deposition, following adding 2 μL of liposome solution, Tris-HCl buffer (1 μL, 20 mM, pH 8.8) was dropped on the mica surface and incubated for 10 min. The undeposited liposomes were then removed by rinsing with Milli-Q water (20 μL × 5). For the AFM observations, liposomes were immersed in a liquid cell filled with buffer A (20 mM Tris-HCl, pH 8.0, 30 mM KCl, 2 mM $MgCl_2$).

Serum Stability and *In Vitro* Drug Release. Five hundred microliters of liposomes (5 mg/mL) was added to 500 μL of serum and incubated at 37 °C. Then, the size, polydispersity index, and zeta-potential of the incubated liposomes were analyzed every 20 min. Similarly, 400 μL of HCPT-loaded liposomes was added to 1600 μL of FBS and incubated at 37 °C in a water bath. At the determined time points, 100 μL samples were withdrawn and then centrifuged at 8000 rpm for 10 min. The supernatant was carefully collected. HCPT was extracted by the addition of a 1:1 ratio of supernatant and acetonitrile, followed by vortexing and then centrifugation at 10 000 rpm. The organic phase was carefully collected for HPLC analysis. The mobile phase was a mixture of methanol and 0.05 M ammonium acetate at a ratio of 55:45. Twenty microliters of supernatant was injected into the HPLC system. Analysis was performed with C18 at 25 °C, and the detection wavelength was 266 nm.

Cellular Uptake. For the cellular uptake study, we selected two cancer model cell lines: BxPC-3 and HPSC Huh-7. Each kind of tumor cell was seeded at a density of 10^4 cells/well in 24-well plates and incubated for 24 h. Liposomes labeled with the fluorescent DiI probe were used to investigate the uptake efficiency. Cells were incubated with liposome suspensions (1 mg/mL) for 2 h at 37 °C. Cells were washed with PBS three times and fixed with polyformaldehyde for 20 min. DAPI solution was added to the cell culture and incubated for 20 min at room temperature. Then, the samples were imaged by CLSM.

Cytotoxicity Study. The cytotoxicity of liposomes to BxPC-3 and HPSC cells was measured by the MTT assay. BxPC-3 and HPSC cells were seeded separately in a 96-well plate at a density of 5 × 10^3 cells/well. The liposome concentration was varied from 0.025 to 1.0 mg/mL at six different values, three wells for each value. The HCPT concentration varied from 0.1 to 100 μg/mL. The whole plate was incubated at 37 °C for 24 h. Then, the supernatant was discarded, and 100 μL of MTT solution (5 mg/mL in water) was added to each well. The plate was further incubated for 4 h at 37 °C. Then, the medium was removed, and the cells were lysed by the addition of 150 μL of dimethyl sulfoxide. The absorbance was measured by using an H1m microplate

DOI: 10.1021/acsnano.9b01181
ACS Nano 2019, 13, 7676−7689

reader at 490 nm. Cell viability (%) was calculated as $A_{test}/A_{control} \times 100\%$, where A_{test} and $A_{control}$ represented the absorbance of cells treated with test solutions and blank culture media, respectively.

BxPC-3 and HPSC Multicellular Spheroids. By using a lipid overlay system as described previously,[32] we established the BxPC-3 and HPSC MCSs. In brief, 2% (w/v) sterilized agarose solution (200 μL) was dropped into each well of 48-cell culture plates, followed by seeding with 5000 BxPC-3 and 5000 HPSC cells. Then, the BxPC-3 and HPSC MCSs were allowed to grow for 7 days (37 °C, 5% CO_2).

Liposome Penetration, Deformation, and Movement in MCSs. MCSs were added into the ultra-low-attachment 24-well plates. The DiI-labeled liposomes in DMEM (1 mg/mL, pH 7.0) were then added into the plates. The MCSs were harvested after 2 h, washed with PBS (pH 7.4, 0.01 M) three times, and imaged by CLSM or STED microscopy.

Preparation of Collagen(I) Hydrogels. Collagen hydrogels (1.5 mg/mL) were constructed to mimic the ECM structure. First, bovine collagen(I) solution (2.4 mg/mL, 300 μL) was mixed with PBS (10×, 50 μL), sodium hydroxide (0.1 M, 10 μL), and RPMI medium (containing 10% fetal bovine serum and 1% penicillin−streptomycin, 120 μL) and was kept cool on ice. Next, the mixture was kept at 37 °C for 4 h to ensure the assembly of the intact collagen(I) matrix.

Scanning Electron Microscopy. SEM examination of the ultrastructure of the tumor ECM was performed as previously described.[45] Briefly, glutaraldehyde-fixed samples were treated with 1% osmium tetroxide, rinsed in distilled water, and dehydrated in solutions with increasing alcohol concentrations. The samples were then critical-point dried, sputter-coated with gold, and investigated with a Nova NanoSEM 230 microscope (FEI Co., Hillsboro, OR).

Multiple Particle Tracking. The *ex vivo* tracking studies were exploited as previously reported.[46] Briefly, 5 μL of liposomes was carefully pipetted onto 200 μL of collagen(I) hydrogels and incubated for 30 min before microscopy. Movies were captured for 10 s using a fluorescence microscope. The temporal resolution was 32.6 ms, and the tracking resolution was 10 nm. The trajectories for 300 particles were analyzed using ImageJ. The time-averaged mean square displacement (MSD) and effective diffusivity (D_{eff}) were calculated as

$$\mathrm{MSD}_t = (x_t - x_0)^2 + (y_t - y_0)^2 \text{ and } D_{\mathrm{eff}} = \mathrm{MSD}/(4t)$$

where x and y represent the coordinates of the particle and t indicates the time scale.

Immunofluorescence Staining. The MCSs were sliced, fixed, and permeabilized. The primary antibodies were then dropped onto the slices and co-incubated at 4 °C for 8 h. After being washed, the MCSs were stained with anti-rabbit IgG Alexa Fluor 488 secondary antibody (1:500) for 1 h. The nuclei were stained with DAPI and then analyzed by using a Leica SP8 microscope.

Tumor Penetration by *In Vivo* Imaging. The subcutaneous-tumor-bearing nude mouse model was established by subcutaneous injection of BxPC-3 and HPSC cells (n = 5). Tumors were used when they reached approximately 5 mm in diameter. IR783 was incorporated into liposomes as a fluorescence indicator. Lip2, Lip3, Lip3, and Lip4 (100 μL) with 40 μg/mL IR783 were peritumorally injected into the mice. *In vivo* radioactive optical imaging was performed with an IVIS 100 Spectrum system. The mice were placed in a light-tight chamber under isoflurane anesthesia, and luminescent images were captured at the determined time points. The Living Image 3.1 software was used to analyze to images.

Tumor Penetration Study *in Vivo*. DSPE-PEG2000-FITC or DiI-labeled Lip2, Lip3, Lip4, and Lip5 were first peritumorally injected into BxPC-3-HPSC-bearing nude mice (n = 5). The nude mice were sacrificed 2 h postinjection. The tumor tissues were excised, washed, and sliced. The tumor slices were then incubated with α-SMA overnight at 4 °C, followed by incubation with anti-rabbit IgG Alexa Fluor 555 secondary antibody (1:500) or anti-rabbit IgG Alexa Fluor 488 secondary antibody (1:500) at room temperature for 1 h. The nuclei were stained with DAPI for 30 min. After being sealed with 90% glycerol, the samples were observed by CLSM with a 10× objective. For the different depth of tumor penetration study *in vivo*, samples were observed by Leica DM 6B with a 10× objective, and the whole section images were obtained by merging tile-scanned images.

***In Vivo* Pharmacodynamics Experiments.** For the *in vivo* tumor suppression experiment, the nude mice were peritumorally injected with PBS or HCPT-loaded liposomal formulations (control, Lip2, Lip3, Lip4, and Lip5) at an equivalent HCPT dose of 2.0 mg/kg of mouse body weight. The mice received injections on days 3, 6, 9, 12, 15, and 18 until the tumor volume reached 100−200 mm^3. Tumor growth was monitored by measuring the perpendicular diameter of the tumor using calipers. At the end of the experiment, the animals were sacrificed, and the tumor tissue was removed, weighed, and fixed with 4% paraformaldehyde for 48 h. All samples were dehydrated using an automatic dehydrator (Shandon Excelsior ES, Thermo, USA) and embedded in a wax block (HISTOSTABR). A 3 μm thick paraffin section (LEICARM2245) was prepared, stained with hematoxylin and Titan red (Varistain Gemini ES), and mounted (Shandon Clearvue). Tumor cell apoptosis and necrosis were observed under a 20× microscope.

Statistical Analysis. All the data are reported as the means ± SD. Student's t-test was used when two groups were compared, and one-way analysis of variance (ANOVA) with Tukey's post-hoc test was used when multiple groups were compared ($P > 0.05$, ns; $^*P < 0.05$; $^{**}P < 0.01$; $^{***}P < 0.001$, $^{****}P < 0.0001$).

ASSOCIATED CONTENT

Supporting Information

The Supporting Information is available free of charge on the ACS Publications website at DOI: 10.1021/acsnano.9b01181.

Physical properties of the liposomes, selected equilibrium configurations of vesicles composed of Lip2, Lip5, and Lip6 at different indentation depths, cytotoxicity of liposomes, SEM images of collagen(I) hydrogels, intratumor penetration, and distribution of DiI-labeled liposomes (PDF)

Movie S1: diffusion and transformation of Lip2 in BxPC-3-HPSC MCSs captured by a gSTED microscope (T = 37 °C) (AVI)

Movie S2: diffusion and transformation of Lip3 in BxPC-3-HPSC MCSs captured by a gSTED microscope (T = 37 °C) (AVI)

Movie S3: diffusion and transformation of Lip4 in BxPC-3-HPSC MCSs captured by a gSTED microscope (T = 37 °C) (AVI)

Movie S4: diffusion and transformation of Lip5 in BxPC-3-HPSC MCSs captured by a gSTED microscope (T = 37 °C) (AVI)

AUTHOR INFORMATION

Corresponding Authors

*E-mail: xyi@pku.edu.cn.
*E-mail: ellewang@163.com.
*E-mail: ygan@simm.ac.cn.

ORCID

Xin Yi: 0000-0002-4726-5765
Yong Gan: 0000-0002-4579-994X

Author Contributions

#Z.D. and M.Y. contributed equally to this work.

Notes

The authors declare no competing financial interest.

ACKNOWLEDGMENTS

We are grateful for the financial support from the National Natural Science Foundation of China (81803445 to M.Y.,

DOI: 10.1021/acsnano.9b01181
ACS Nano 2019, 13, 7676−7689

81573571 to R.W., 11872005 to X.Y., 81573378 and 81773651 to Y.G.). This work was also supported by the Excellent Academic Leaders Program of Shanghai (16XD1403500), the Science and Technology Commission of Shanghai Municipality (17430741500), the Shanghai Science and Technology Committee (18430721600), the program of the Shanghai E-Research Institute of Bioactive Constituents in Traditional Chinese Medicine, the K.C. Wong Education Foundation, and the New Star Program, Shanghai Institute of Materia Medica, CAS. We would like to thank Zhi Liu from the National Center for Protein Science Shanghai for the cryo-EM data, Yuanyuan Su from the Leica Microscopy Laboratory in Shanghai for the data from Leica SP8 with STED, and Huiqin Li from the Instrumental Analysis Center of Shanghai Jiao Tong University for the AFM data.

REFERENCES

(1) Colombo, M.; Raposo, G.; Thery, C. Biogenesis, Secretion, and Intercellular Interactions of Exosomes and Other Extracellular Vesicles. *Annu. Rev. Cell Dev. Biol.* **2014**, *30*, 255−289.

(2) Vorselen, D.; MacKintosh, F. C.; Roos, W. H.; Wuite, G. J. Competition Between Bending and Internal Pressure Governs the Mechanics of Fluid Nanovesicles. *ACS Nano* **2017**, *11*, 2628−2636.

(3) Doktorova, M.; Harries, D.; Khelashvili, G. Determination of Bending Rigidity and Tilt Modulus of Lipid Membranes from Real-Space Fluctuation Analysis of Molecular Dynamics Simulations. *Phys. Chem. Chem. Phys.* **2017**, *19*, 16806−16818.

(4) Et-Thakafy, O.; Delorme, N.; Guyomarc'h, F.; Lopez, C. Mechanical Properties of Milk Sphingomyelin Bilayer Membranes in the Gel Phase: Effects of Naturally Complex Heterogeneity, Saturation and Acyl Chain Length Investigated on Liposomes Using AFM. *Chem. Phys. Lipids* **2018**, *210*, 47−59.

(5) Rudd, A. K.; Devaraj, N. K. Traceless Synthesis of Ceramides in Living Cells Reveals Saturation-Dependent Apoptotic Effects. *Proc. Natl. Acad. Sci. U. S. A.* **2018**, *115*, 7485−7490.

(6) Purushothaman, S.; Cicuta, P.; Ces, O.; Brooks, N. J. Influence of High Pressure on the Bending Rigidity of Model Membranes. *J. Phys. Chem. B* **2015**, *119*, 9805−9810.

(7) Stowell, M. H.; Marks, B.; Wigge, P.; McMahon, H. T. Nucleotide-Dependent Conformational Changes in Dynamin: Evidence for a Mechanochemical Molecular Spring. *Nat. Cell Biol.* **1999**, *1*, 27−32.

(8) Lipowsky, R. Remodeling of Membrane Compartments: Some Consequences of Membrane Fluidity. *Biol. Chem.* **2014**, *395*, 253−274.

(9) Neubauer, M. P.; Poehlmann, M.; Fery, A. Microcapsule Mechanics: From Stability to Function. *Adv. Colloid Interface Sci.* **2014**, *207*, 65−80.

(10) Best, J. P.; Yan, Y.; Caruso, F. The Role of Particle Geometry and Mechanics in the Biological Domain. *Adv. Healthcare Mater.* **2012**, *1*, 35−47.

(11) Anselmo, A. C.; Mitragotri, S. Impact of Particle Elasticity on Particle-Based Drug Delivery Systems. *Adv. Drug Delivery Rev.* **2017**, *108*, 51−67.

(12) Guo, P.; Liu, D.; Subramanyam, K.; Wang, B.; Yang, J.; Huang, J.; Auguste, D. T.; Moses, M. A. Nanoparticle Elasticity Directs Tumor Uptake. *Nat. Commun.* **2018**, *9*, 130.

(13) Hinde, E.; Thammasiraphop, K.; Duong, H. T.; Yeow, J.; Karagoz, B.; Boyer, C.; Gooding, J. J.; Gaus, K. Pair Correlation Microscopy Rveals the Role of Nanoparticle Shape in Intracellular Transport and Site of Drug Release. *Nat. Nanotechnol.* **2017**, *12*, 81−89.

(14) Mo, R.; Jiang, T.; Gu, Z. Enhanced Anticancer Efficacy by ATP-Mediated Liposomal Drug Delivery. *Angew. Chem., Int. Ed.* **2014**, *53*, 5815−5820.

(15) Hu, X.; Zhang, Y.; Xie, Z.; Jing, X.; Bellotti, A.; Gu, Z. Stimuli-Responsive Polymersomes for Biomedical Applications. *Biomacromolecules* **2017**, *18*, 649−673.

(16) Et-Thakafy, O.; Delorme, N.; Gaillard, C.; Meriadec, C.; Artzner, F.; Lopez, C.; Guyomarc'h, F. Mechanical Properties of Membranes Composed of Gel-Phase or Fluid-Phase Phospholipids Probed on Liposomes by Atomic Force Spectroscopy. *Langmuir* **2017**, *33*, 5117−5126.

(17) Yi, X.; Gao, H. Cell Membrane Wrapping of a Spherical Thin Elastic Shell. *Soft Matter* **2015**, *11*, 1107−1115.

(18) Steltenkamp, S.; Muller, M. M.; Deserno, M.; Hennesthal, C.; Steinem, C.; Janshoff, A. Mechanical Properties of Pore-Spanning Lipid Bilayers Probed by Atomic Force Microscopy. *Biophys. J.* **2006**, *91*, 217−226.

(19) Cabral, H.; Matsumoto, Y.; Mizuno, K.; Chen, Q.; Murakami, M.; Kimura, M.; Terada, Y.; Kano, M. R.; Miyazono, K.; Uesaka, M.; Nishiyama, N.; Kataoka, K. Accumulation of Sub-100 nm Polymeric Micelles in Poorly Permeable Tumours Depends on Size. *Nat. Nanotechnol.* **2011**, *6*, 815−823.

(20) Cabral, H.; Makino, J.; Matsumoto, Y.; Mi, P.; Wu, H.; Nomoto, T.; Toh, K.; Yamada, N.; Higuchi, Y.; Konishi, S.; Kano, M. R.; Nishihara, H.; Miura, Y.; Nishiyama, N.; Kataoka, K. Systemic Targeting of Lymph Node Metastasis through the Blood Vascular System by Using Size-Controlled Nanocarriers. *ACS Nano* **2015**, *9*, 4957−4967.

(21) Dancy, J. G.; Wadajkar, A. S.; Schneider, C. S.; Mauban, J. R. H.; Goloubeva, O. G.; Woodworth, G. F.; Winkles, J. A.; Kim, A. J. Non-Specific Binding and Steric Hindrance Thresholds for Penetration of Particulate Drug Carriers within Tumor Tissue. *J. Controlled Release* **2016**, *238*, 139−148.

(22) Lieleg, O.; Ribbeck, K. Biological Hydrogels as Selective Diffusion Barriers. *Trends Cell Biol.* **2011**, *21*, 543−551.

(23) Zhang, L.; Feng, Q.; Wang, J.; Zhang, S.; Ding, B.; Wei, Y.; Dong, M.; Ryu, J. Y.; Yoon, T. Y.; Shi, X.; Sun, J.; Jiang, X. Microfluidic Synthesis of Hybrid Nanoparticles with Controlled Lipid Layers: Understanding Flexibility-Regulated Cell-Nanoparticle Interaction. *ACS Nano* **2015**, *9*, 9912−9921.

(24) Anselmo, A. C.; Zhang, M.; Kumar, S.; Vogus, D. R.; Menegatti, S.; Helgeson, M. E.; Mitragotri, S. Elasticity of Nanoparticles Influences their Blood Circulation, Phagocytosis, Endocytosis, and Targeting. *ACS Nano* **2015**, *9*, 3169−3177.

(25) Li, Y.; Zhang, X.; Cao, D. Nanoparticle Hardness Controls the Internalization Pathway for Drug Delivery. *Nanoscale* **2015**, *7*, 2758−2769.

(26) Sun, J.; Zhang, L.; Wang, J.; Feng, Q.; Liu, D.; Yin, Q.; Xu, D.; Wei, Y.; Ding, B.; Shi, X.; Jiang, X. Tunable Rigidity of (Polymeric Core)-(Lipid Shell) Nanoparticles for Regulated Cellular Uptake. *Adv. Mater.* **2015**, *27*, 1402−1407.

(27) Yi, X.; Shi, X.; Gao, H. Cellular Uptake of Elastic Nanoparticles. *Phys. Rev. Lett.* **2011**, *107*, 098101.

(28) Abbott, A. Cell Culture: Biology's New Dimension. *Nature* **2003**, *424*, 870−872.

(29) Suzuki, H.; Bae, Y. H. Evaluation of Drug Penetration with Cationic Micelles and Their Penetration Mechanism Using an *In Vitro* Tumor Model. *Biomaterials* **2016**, *98*, 120−130.

(30) Mahadevan, D.; Von Hoff, D. D. Tumor-Stroma Interactions in Pancreatic Ductal Adenocarcinoma. *Mol. Cancer Ther.* **2007**, *6*, 1186−1197.

(31) Apte, M. V.; Wilson, J. S.; Lugea, A.; Pandol, S. J. A Starring Role for Stellate Cells in the Pancreatic Cancer Microenvironment. *Gastroenterology* **2013**, *144*, 1210−1219.

(32) Li, H. J.; Du, J. Z.; Liu, J.; Du, X. J.; Shen, S.; Zhu, Y. H.; Wang, X.; Ye, X.; Nie, S.; Wang, J. Smart Superstructures with Ultrahigh pH-Sensitivity for Targeting Acidic Tumor Microenvironment: Instantaneous Size Switching and Improved Tumor Penetration. *ACS Nano* **2016**, *10*, 6753−6761.

(33) Apte, M. V.; Park, S.; Phillips, P. A.; Santucci, N.; Goldstein, D.; Kumar, R. K.; Ramm, G. A.; Buchler, M.; Friess, H.; McCarroll, J. A.; Keogh, G.; Merrett, N.; Pirola, R.; Wilson, J. S. Desmoplastic Reaction in Pancreatic Cancer: Role of Pancreatic Stellate Cells. *Pancreas* **2004**, *29*, 179−187.

(34) Han, X.; Li, Y.; Xu, Y.; Zhao, X.; Zhang, Y.; Yang, X.; Wang, Y.; Zhao, R.; Anderson, G. J.; Zhao, Y.; Nie, G. Reversal of Pancreatic

DOI: 10.1021/acsnano.9b01181
ACS Nano 2019, 13, 7676−7689

Desmoplasia by Re-Educating Stellate Cells with a Tumour Microenvironment-Activated Nanosystem. *Nat. Commun.* **2018**, *9*, 3390.
(35) Zhao, W.; Ajani, J. A.; Sushovan, G.; Ochi, N.; Hwang, R.; Hafley, M.; Johnson, R. L.; Bresalier, R. S.; Logsdon, C. D.; Zhang, Z.; Song, S. Galectin-3 Mediates Tumor Cell-Stroma Interactions by Activating Pancreatic Stellate Cells to Produce Cytokines *via* Integrin Signaling. *Gastroenterology* **2018**, *154*, 1524−1537.
(36) Ikenaga, N.; Ohuchida, K.; Mizumoto, K.; Cui, L.; Kayashima, T.; Morimatsu, K.; Moriyama, T.; Nakata, K.; Fujita, H.; Tanaka, M. CD10+ Pancreatic Stellate Cells Enhance The Progression of Pancreatic Cancer. *Gastroenterology* **2010**, *139*, 1041−1051.
(37) Hu, Q.; Gao, X.; Gu, G.; Kang, T.; Tu, Y.; Liu, Z.; Song, Q.; Yao, L.; Pang, Z.; Jiang, X.; Chen, H.; Chen, J. Glioma Therapy Using Tumor Homing and Penetrating Peptide-Functionalized PEG-PLA Nanoparticles Loaded with Paclitaxel. *Biomaterials* **2013**, *34*, 5640−5650.
(38) Takechi-Haraya, Y.; Goda, Y.; Sakai-Kato, K. Control of Liposomal Penetration into Three-Dimensional Multicellular Tumor Spheroids by Modulating Liposomal Membrane Rigidity. *Mol. Pharmaceutics* **2017**, *14*, 2158−2165.
(39) Yu, M.; Wang, J.; Yang, Y.; Zhu, C.; Su, Q.; Guo, S.; Sun, J.; Gan, Y.; Shi, X.; Gao, H. Rotation-Facilitated Rapid Transport of Nanorods in Mucosal Tissues. *Nano Lett.* **2016**, *16*, 7176−7182.
(40) Yu, M.; Xu, L.; Tian, F.; Su, Q.; Zheng, N.; Yang, Y.; Wang, J.; Wang, A.; Zhu, C.; Guo, S.; Zhang, X.; Gan, Y.; Shi, X.; Gao, H. Rapid Transport of Deformation-Tuned Nnoparticles Across Biological Hydrogels and Cellular Barriers. *Nat. Commun.* **2018**, *9*, 2607.
(41) Wang, J. L.; Yang, Y. W.; Yu, M. R.; Hu, G. Q.; Gan, Y.; Gao, H. J.; Shi, X. H. Diffusion of Rod-Like Nanoparticles in Non-Adhesive and Adhesive Porous Polymeric Gels. *J. Mech. Phys. Solids* **2018**, *112*, 431−457.
(42) Sun, Q.; Zhou, Z.; Qiu, N.; Shen, Y. Rational Design of Cancer Nanomedicine: Nanoproperty Integration and Synchronization. *Adv. Mater.* **2017**, *29*, 1606628.
(43) Cevc, G.; Schatzlein, A. G.; Richardsen, H.; Vierl, U. Overcoming Semipermeable Barriers, Such As The Skin, With Ultradeformable Mixed Lipid Vesicles, Transfersomes, Liposomes, or Mixed Lipid Micelles. *Langmuir* **2003**, *19*, 10753−10763.
(44) Cevc, G.; Richardsen, H. Lipid Vesicles and Membrane Fusion. *Adv. Drug Delivery Rev.* **1999**, *38*, 207−232.
(45) Ji, T.; Lang, J.; Wang, J.; Cai, R.; Zhang, Y.; Qi, F.; Zhang, L.; Zhao, X.; Wu, W.; Hao, J.; Qin, Z.; Zhao, Y.; Nie, G. Designing Liposomes To Suppress Extracellular Matrix Expression To Enhance Drug Penetration and Pancreatic Tumor Therapy. *ACS Nano* **2017**, *11*, 8668−8678.
(46) Huang, X.; Chisholm, J.; Zhuang, J.; Xiao, Y.; Duncan, G.; Chen, X.; Suk, J. S.; Hanes, J. Protein Nanocages that Penetrate Airway Mucus and Tumor Tissue. *Proc. Natl. Acad. Sci. U. S. A.* **2017**, *114*, E6595−E6602.

DOI: 10.1021/acsnano.9b01181
ACS Nano 2019, 13, 7676−7689